The Astrophysical Journal, 725:319–330, 2010 December 10 doi:10.1088/0004-637X/725/1/319

RECONNECTION AND ENERGETICS IN TWO-RIBBON FLARES: A REVISIT OF THE BASTILLE-DAY FLARE

Jiong Qiu[1], WenJuan Liu[1], Nicholas Hill[2], and Maria Kazachenko[1]
[1] Department of Physics, Montana State University, Bozeman, MT 59717-3840, USA
[2] Department of Astronomy, University of Wisconsin Madison, Madison, WI 53706, USA
Received 2010 August 19; accepted 2010 September 26; published 2010 November 18

ABSTRACT

We conduct a semi-quantitative analysis of two-ribbon flares to investigate the observational relationship between magnetic reconnection and energetics by revisiting the Bastille-day flare, particularly the UV and hard X-ray (HXR) observations. The analysis establishes that prominent UV emission is primarily produced by precipitating electrons that also produce HXRs. In addition, reconnection and subsequent energy release along adjacent field lines along the polarity inversion line (PIL) combined with elongated decay of UV emission may account for the observed extended UV ribbons whereas HXR sources with rapid decay appear mostly as compact kernels. Observations also show that HXR sources and UV brightenings exhibit an organized parallel motion along the magnetic PIL during the rise of the flare, and then the perpendicular expansion of UV ribbons dominate during the peak. With a 2.5 dimensional approximation with the assumed translational dimension along the PIL, we derive geometric properties of UV ribbons and infer the pattern of reconnection as with a varying magnetic guide field during reconnection. It is shown that HXR and UV emissions evolve in a similar way to reconnection rates determined by the perpendicular "motion." The analysis suggests that a relatively strong guide field may be present during the rise of the flare, whereas particle acceleration and non-thermal energy release are probably more efficient with an enhanced reconnection rate with a relatively weak guide field. We discuss the role of the guide field in reconnection and particle energization, as well as novel observational experiments that may be conducted to shed new light on these issues.

Key words: magnetic reconnection – Sun: X-rays, gamma rays

Online-only material: color figure

1. INTRODUCTION

Magnetic reconnection is the commonly accepted mechanism that governs energy release in solar flares. Reconnection allows a change of connectivity between magnetic structures and therefore the overall topology and magnetic energy in the field. In a wider sense, it is understood that the post-reconnection magnetic field contains less energy than the pre-reconnection configuration, and the excess of magnetic energy is released in various forms in heating plasmas, accelerating charged particles, and accelerating bulk plasmas such as reconnection outflow or jets. Occurrence of fast reconnection requires that reconnection takes place locally where non-ideal effects are important. Traditional issues related to reconnection physics concern how fast reconnection and subsequent energy release, such as via particle acceleration, take place.

A variety of physical mechanisms have been put forward for reconnection. Clearly the *Spitzer* resistivity in solar corona condition is way too small (by three to four orders of magnitude) to account for fast reconnection evident in solar flares. An anomalous resistivity incorporates microscopic physics that leads to a reconnection electric field (E) associated with fast reconnection. Here, E is equated to the inductive electric field in the inflow region, which can be inferred from flare ribbon evolution to be of order 10^1-10^4 V m^{-1} (Poletto & Kopp 1986; Foukal & Behr 1995; Qiu et al. 2002, 2004; Jing et al. 2005) in a two-dimensional approach. Magnetic reconnection takes place in three dimensions, which means that at the reconnection site, all three components of the magnetic field are usually present. The reconnecting component diminishes at the reconnection site, but there exists a longitudinal component parallel to the inductive electric field, which we call the guide field. The effect of a guide field is complex. Since particles are magnetized, the collision rate is significantly reduced; a strong guide field also increases the magnetic pressure in the current sheet, which may work against the reconnection inflow. On the other hand, a guide field may trigger fast reconnection when non-resistive terms in the general Ohm's law are in play (the Hall term, for example), or the turbulence such as that caused by the two-stream instability due to the separation of electrons from protons along the guide field (Drake et al. 2006).

Observationally determining the guide field is a difficult problem, which requires knowledge of the three-dimensional geometry of the magnetic field in the corona. However, in typical two-ribbon flares, it is frequently seen that the ribbons form along the PIL, suggesting that we may by and large treat the geometry as 2.5 dimensions relative to the PIL and study the flare ribbon evolution to infer the reconnection pattern, including deciphering the guide field. In a good number of two-ribbon flares (e.g., Kitahara & Kurokawa 1990; Moore et al. 2001; Su et al. 2007; Lee & Gary 2008; Qiu 2009), it is shown that flare ribbons to a large degree follow the shape of the PIL; also, more importantly, the ribbon brightening starts with a parallel motion and is later dominated by a perpendicular motion in an organized pattern. This organization suggests that reconnection may be described reasonably in a 2.5 dimensional approximation with a "guide" direction along the PIL, with respect to which it is possible to measure the reconnection rate.

In this paper, we revisit the well-known Bastille-day two-ribbon flare observed in UV and hard X-rays (HXRs). The UV observations, due to their high spatial resolution, are used to analyze the reconnection pattern, while HXRs are generally used as proxies for electron properties. Furthermore, it has been known that, whereas UV and optical observations of two-ribbon flares exhibit extended flare ribbons, HXR sources are usually mapped as compact and localized kernels (Sakao

1994; Krucker et al. 2005; Bogachev et al. 2005; DesJardins 2007; Grigis & Benz 2008). The solution to this longstanding puzzle is key to understanding the three-dimensional nature of magnetic reconnection and energy release (e.g., Birn et al. 2009). It is therefore clear that illuminating the relationship between reconnection and (non-thermal) energetics requires understanding the relationship between HXR and UV emissions. These are the two issues we strive to address in this study.

2. OVERVIEW OF THE OBSERVATION

The flare in the present paper is the well-known Bastille-day flare which occurred at 10:00 UT on 2000 July 14. The flare was observed by *Yohkoh* and *TRACE* (Handy et al. 1999). The *Yohkoh* observation of this event during 10:13–10:20 UT was lost (A. Takeda 2010, private communication), and only covered the second phase of the flare from 10:20 UT, and *TRACE* observed the event in UV 1600 Å continuum as well as in the EUV bands for its entire duration. Studies of this flare can be found in many research papers (see Solar Physics Special Issue 2001) and in particular in Fletcher & Hudson (2001). In this paper, we re-examine this event observed in the UV 1600 Å continuum, which has a 20–40 s cadence and 0.″5 pixel scale, and in the HXR observations of $\geqslant$20 keV by the *Yohkoh Hard X-ray Telescope* (*HXT*; Kosugi et al. 1990), with the motivation to investigate the relationship between magnetic reconnection and (non-thermal) energetics.

Figure 1 gives an overview of the flare evolution in HXR and UV wavelengths, superimposed on the co-aligned longitudinal magnetogram obtained by MDI about 30 minutes before the flare onset. In the figure, the magnetogram is shown to be partitioned into individual magnetic cells, based on which the coronal magnetic field topology may be computed (Barnes et al. 2005; Longcope et al. 2007; Kazachenko et al. 2009). In Figure 1(a), the HXR images are reconstructed using the maximum entropy method built in the standard SolarSoftware package (Sato et al. 1999). It is seen that $\geqslant$20 keV HXR emission of the flare usually exhibits two to three compact sources in magnetic fields of opposite polarities. During the flare evolution, the HXR sources gradually shift, nearly along the magnetic polarity inversion line (PIL), from the western part of the active region to the eastern part. Figure 1(b) shows a similar pattern of flare evolution in the UV continuum. At this wavelength, the flare exhibits well-defined two ribbons, with their shapes outlined by the curved PIL. From the figure, it is also apparent that the flare is composed of two phases, during which energy release takes place at two locations of the active region. During the first phase before 10:25 UT, two ribbons develop in the western portion of the active region, and after 10:25 UT, the flare takes place in the eastern portion of the active region. Note that the $\geqslant$20 keV HXR emission and the UV continuum emission both originate from the lower transition region or upper chromosphere, which is impulsively heated during the flare. They reflect the feet of a post-flare loop arcade, better seen in EUV and soft X-ray emissions, formed by magnetic reconnection in the corona.

Figure 2 shows the light curves of the flare observed in HXR at two energy channels (M1: 23–33 keV, and M2: 33–53 keV), UV 1600 Å continuum, and soft X-ray 1–8 Å by *GOES*, as well as the magnetic reconnection rate. The UV light curve is a sum of all counts in the semi-calibrated UV images. The reconnection rate is derived by summing up magnetic flux in newly brightened ribbon pixels per unit time (Fletcher & Hudson 2001; Qiu et al. 2002, 2004; Saba et al. 2006). The detailed procedures of image processing and derivation of the UV

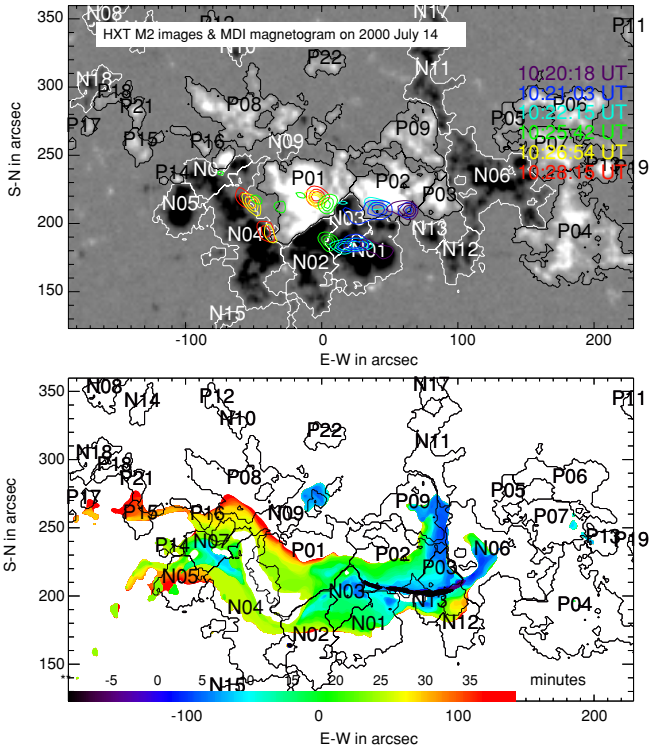

Figure 1. Upper: photospheric magnetogram from MDI superimposed with the contours of HXR images obtained by HXT M2 channel (33–53 keV). Lower: temporal and spatial evolution of the UV flare ribbon. Time is indicated by the color code.

(A color version of this figure is available in the online journal.)

light curve and reconnection rate will be described in the next section.

Some interesting facts can be observed from these overview figures. First, the well-defined UV two-ribbon morphology, at first glance, reflects a nearly two-dimensional picture of solar flares; however, the temporal evolution of the ribbon indicates that the flare ribbon is brightened nearly sequentially along the PIL (the so-called "zipper effect"), which is not a two-dimensional process. Furthermore, the HXR sources are compact and localized, and this well-known discrepancy between HXR and UV maps is considered to reflect the three-dimensional nature of two-ribbon flares. Second, it is also noted that UV emission (total counts) evolves along with $\geqslant$20 keV HXRs, but it decays more slowly. The coincident rise in UV and HXR emissions is generally understood to imply that UV and HXR are both produced due to heating of the lower atmosphere primarily by precipitating non-thermal electrons. But the slow decay in UV emission may be an effect of either slow cooling or continuous heating in a gradual manner, which is not directly related to the non-thermal electrons responsible for HXRs. Third, though the reconnection rate in general evolves along with the emission curves, it peaks well before the HXR emission, unlike what is reported in some other events when the reconnection rate well tracks the HXR emission during the rise, peak, and decay (e.g., Qiu et al. 2004). This may suggest that the brightening has taken place but the heating rate is low during the rise of the flare. Note that these displayed fluxes are all extensive quantities, so the lack of correlation means that the energy release flux per unit reconnected flux varies with time. Since at different stages of the flare, reconnection may take place at different locations between different magnetic structures, this

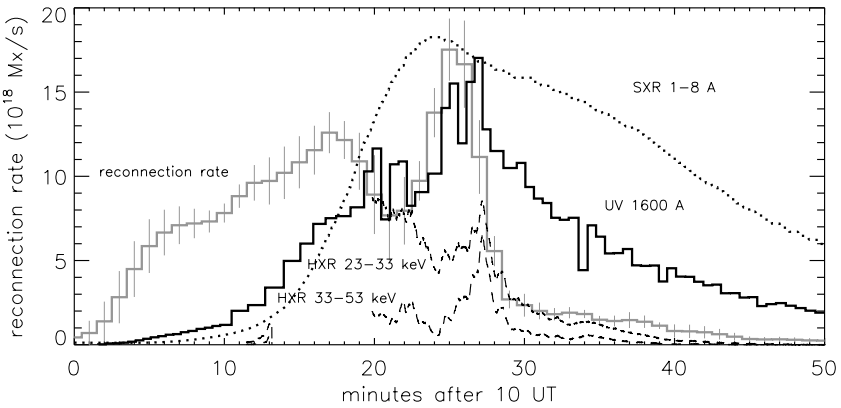

Figure 2. Time profiles of HXRs (dark dashed lines) from HXT M1 (23–33 keV) and M2 (33–53 keV) channels, UV 1600 Å total counts (dark solid lines) by *TRACE*, soft X-ray flux at 1–8 Å by *GOES* (dark dotted lines), and reconnection rate (gray solid lines). The HXR, SXR, and UV light curves are arbitrarily normalized.

discrepancy also says that the efficiency of (non-thermal) energy release as a consequence of reconnection between different magnetic structures is not homogeneous.

These observations raise important questions that will be addressed in the present study. First, what is the relationship between HXR and UV signatures. Second, how is instantaneous flare energy release (specifically in the form of non-thermal electrons) related to magnetic reconnection in a manner other than the two-dimensional description? These two questions are indeed related to each other. The first question also involves understanding the physics of how the lower atmosphere is heated and then emits in the UV continuum, which ultimately has to be investigated through a radiative transfer modeling approach. In the present study, though, it is pragmatically important in the sense that UV images acquired with very high resolution (about 1″) allow us to map and spatially resolve the instantaneous energy release. If at least the phenomenological relationship between UV and HXR can be established, the UV imaging capability will be able to provide another means of diagnosing electron precipitation complementary to HXR observations, which give diagnostics of electron properties but with limited spatial resolution. In the following sections, we will explore ways to establish a relationship between UV and HXRs, as well as energy release and the reconnection pattern.

3. ANALYSIS OF UV IMAGES

3.1. Semi-calibration of UV Images

There is a great advantage of using UV images to follow the morphology evolution with their high resolution (0.″5 pixel scale) and moderate temporal cadence (20–40 s in this event). In order to also extract photometry information, we perform a first-order calibration of UV images taken with different exposures. The UV 1600 Å images are first processed using the trace_prep.pro program that is built into the SolarSoftware package. This program subtracts a nominal dark current value from the images, which are then normalized to the flat field and exposure times. Ideally, the properly processed images should yield the same median counts value, which is determined by the quiescent background in the field of view, throughout the duration of the flare and regardless of the exposures. It is found, however, that the median value of the quiescent background exhibits very large variations nearly anti-correlated with the exposure time, which suggests that an off-set in the nominal dark current pedestal value is present, and it can cause very large erroneous counts when divided by a short exposure time. To find this offset, we fit the background median as a linear function of $1/\tau_{\rm exp}$, where $\tau_{\rm exp}$ is the exposure time of the image. A linear trend of the scatter plot is clearly present as seen in Figure 3(a), indicating the existence of a constant (to first order) dark current offset. This offset is obtained as the slope of the least-square fit and then subtracted from the prepared images. The first-order correction substantially improves the median background, which is then used to normalize the images.

With the semi-calibrated images, the UV emission light curve shown in Figure 2 is obtained by summing up counts from all pixels in each image. The reconnection flux is obtained by summing up magnetic flux in newly brightened pixels in each image (Qiu et al. 2002, 2004). We define newly brightened regions as pixels with brightness (in units of counts) greater than a threshold value of the quiescent median. From the pixel brightness histogram seen in Figure 3(b), the empirical threshold for flare brightening is taken to range from 6 to 10 (note that the intensity distribution of the steady plage brightening usually peaks at 3.5). To minimize uncertainties due to non-physical features (such as cosmic ray pixels) and inconsistent correction of offsets caused by second-order effects of varying exposures or dark pedestal (see the scattering in Figure 3(a)), we also require that the UV brightening should be persistent in a few consecutive time frames. This is justified by the intrinsic long "cooling" time of UV counts in each flaring pixel as evident in the experiment in the next section. All things considered, the maximum uncertainty in the reconnection rate measurement is about 20%–30% of the measured values, as indicated by vertical bars in Figure 3. We also note that the uncertainty is largely dominated by imbalanced fluxes measured from positive and negative ribbons (also see Fletcher & Hudson 2001).

3.2. Decay of UV Emission

Comparison of the UV total counts and HXR light curves suggests that flare ribbon pixels are heated nearly instantaneously (given the time cadence of 20–40 s), likely by particle precipitation, and then undergo a gradual smooth decay. It is reasonable to assume that the decay phase is dominated by either a genuine cooling or some secondary heating not directly related to particle precipitation which would otherwise produce signatures in HXR light curves. The apparent longer "cooling" time seen in the total UV count flux with respect to the HXR flux (Figure 2) may be caused by either the elongated "cooling" in individual pixels or newly brightened pixels after the decay of the HXR, or both. To find out the cause, we first examine UV emission in individual pixels, as shown in Figure 4. It is seen that UV emission

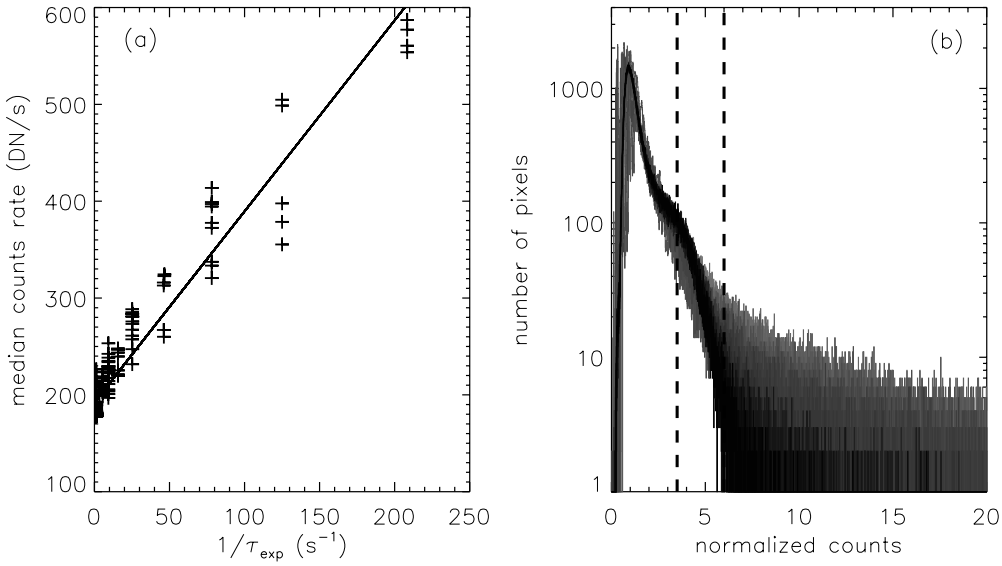

Figure 3. (a) Scatter plot of median counts rate of UV emission vs. $1/\tau_{exp}$, superimposed with the least-square linear fit to the data. The linear trend suggests that an offset of the pedestal dark current value is not properly removed from the UV data (R. E. Nightingale & T. Tarbell 2009, private communication). (b) Histograms of count rates normalized to the median during the flare evolution. The dark color indicates the distribution during the pre-flare, and gray tones indicate the distribution during the flare. The thick dashed vertical line at 3.5 denotes where the plage intensity peaks, and the thick dashed vertical line at 6 denotes where the distribution of flaring image deviates from the pre-flare quiescent image counts distribution.

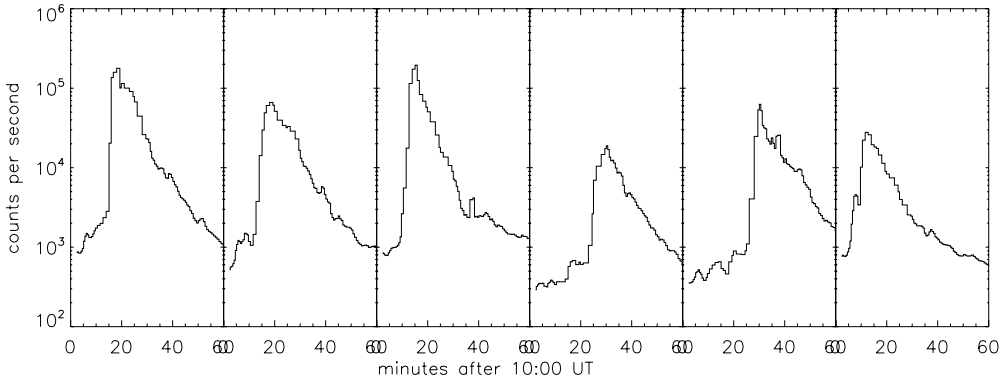

Figure 4. Time profiles of UV counts in individual pixels.

rises rapidly and peaks within two to three time frames (corresponding to 1–2 minutes given the observation cadence), whereas it takes a much longer time to decay. The plots also suggest that the decay of UV emission may be approximated by an exponential function as $C(t) = C_p \exp[-(t - t_p)/\tau_c]$, where C_p is the peak counts, $t - t_p$ is the time after the peak, and τ_c is the characteristic "cooling" time, or the *e*-slope decay time. We fit to this function the decay phase of UV emission in about 7000 pixels which are brightened during the flare. Figure 5 shows the histogram of the *e*-slope decay time from the best-fit pixels, where we empirically define the best fit as occurring when the standard deviation from the fit is within 30% of the measurements. The histogram shows that if we fit the light curve from the peak to 20% of the peak, over 5500 pixels (dark symbols in the figure) can be reasonably fitted by an exponential decay, and if we fit the light curve from the peak to 10% of the maximum, still over 4500 pixels (gray symbols in the figure) are reasonably fitted. The best-fit *e*-slope decay time ranges from 5–10 minutes for the majority of brightened pixels. But keep in mind that τ_c refers to the *e*-slope decay time, not the time it takes for a pixel to cool down to the pre-flare intensity. Figure 5(b) also suggests that τ_c is somewhat anti-correlated with the peak intensity I_p. We consider that the apparent anti-correlation may be an artificial effect caused by the long cadence (∼30 s) of the UV observation, with which shorter decay times are not detected. The apparent decay shown here is governed by the atmosphere heating and cooling mechanisms, convolved with the *TRACE* UV response function.

The analysis suggests that the elongated decay in individual pixels may account for the elongated decay in the total UV counts. Since the HXR observation does not have the capability to track down emission at individual pixels to compare with resolved UV emission, we instead use an empirical method to artificially eliminate the decay of the UV emission in each individual pixel, and then compare the total UV counts from these new images with HXR light curves. The elimination is such that, for each single pixel, we make a mask to only preserve the counts greater than a certain fixed fractional threshold of the peak counts in this pixel, and at other times when the UV counts drop to below this fixed fraction, the counts are reduced to zero. The threshold is empirically determined to be 75%, at which the total UV count light curve compares best with the HXR light curves at ⩾20 keV with the maximum linear cross-correlation (of greater than 90%). Such masked UV images are hereafter called hard UV (HUV) images, since the light curve of this masked image cube is comparable with ⩾20 keV HXRs. Given

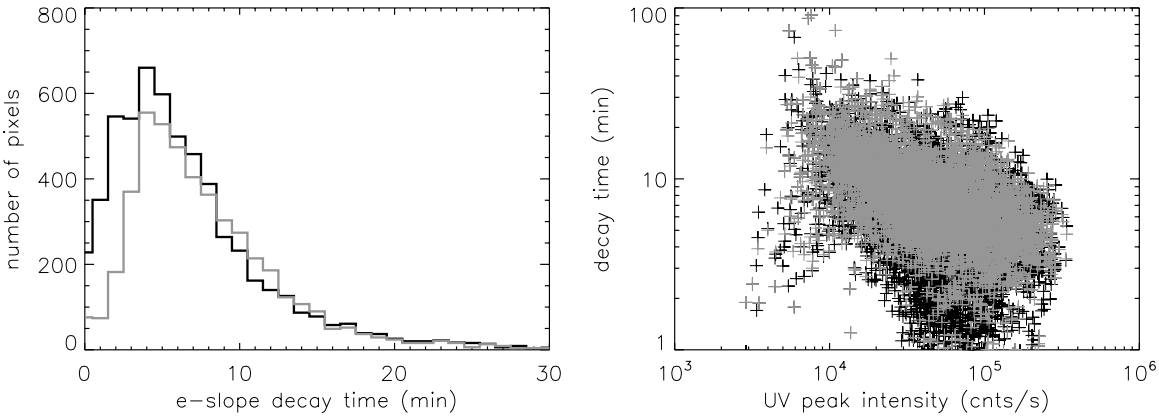

Figure 5. Left: histogram of *e*-slope decay time of UV semi-calibrated counts. Right: *e*-slope decay time vs. peak counts C_p. In both panels, dark symbols (total number of 5500) indicate fitting results with pixels that cool down to 20% of the maximum, and gray symbols (total number of 4500) indicate fitting results with pixels that cool down to 10% of the peak.

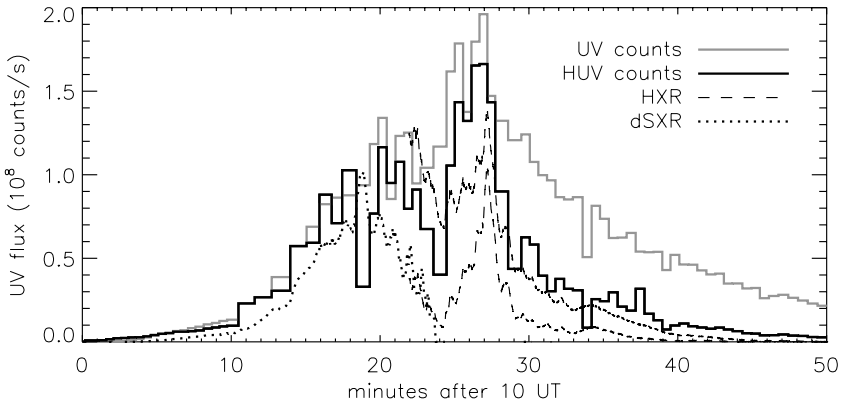

Figure 6. Time profiles of HXRs (dark dashed lines) at M1 (23–33 keV) and M2 (33–53 keV) channels, UV total counts (gray solid lines), HUV counts (dark solid lines; see the text), and time derivative of soft X-ray 1–8 Å flux by *GOES* (dSXR; dark dotted lines). The HUV, HXR, and dSXR light curves are arbitrarily normalized.

the characteristic cooling time, it takes 2–4 minutes to drop to below 75% of the maximum. The cadence of the UV images is 20–40 s, so in the HUV image cube, each pixel is brightened for only a few time frames.

Figure 6 shows the light curve of the original total UV counts as well as the HUV light curve in comparison with the HXR light curves at M1 (23–33 keV) and M2 (33–53 keV) channels. It is seen that the rise and peak of the HUV light curve are hardly modified from the original UV light curve, and the decay becomes much more rapid, which tracks the evolution of $\geqslant$20 keV HXRs. Since *HXT* was not observing during the first phase of the flare before 10:20 UT, we plot the time derivative of the soft X-ray flux obtained by *GOES* at 1–8 Å (hereafter dSXR), which is usually considered to resemble the time evolution of HXRs or microwaves during the rise of the flare (Neupert effect; Neupert 1968). It is seen that the HUV light curve correlates reasonably with the dSXR profile during the first phase. The comparison thus suggests that the UV emission, which rises nearly instantaneously with HXRs (at least during the second phase), is produced primarily by non-thermal electron precipitation, and the long decay in the original UV total counts is not caused by newly brightened pixels during the decay of HXRs, but by the elongated decay of individual pixels which are instantaneously brightened at time scales comparable to HXRs. The experiment also convinces us that such a processed HUV image cube likely reflects sites of instantaneous heating by precipitating electrons, or pseudo HXR images.

In addition, we also examine the semi-quantitative relationship between HUV and $\geqslant$20 keV HXR counts fluxes. The best fit to the scatter plot yields $C_{\rm HUV} \sim C_{\rm HXR}^{0.6\pm0.1}$, where $C_{\rm HXR}$ is the counts flux at HXT M1 (23–33 keV) or M2 (33–53 keV) channels. McClymont & Canfield (1986) found a very similar scaling law as $\phi_E \sim \phi_X^{0.6\pm0.05}$, where ϕ_E and ϕ_X refer to the peak energy fluxes in 10–1030 Å continuum and in $\geqslant$10 keV electrons, respectively, for a few tens of flares. According to McClymont & Canfield (1986), the power index of 0.6 places the atmosphere heating regime in explosive heating by a large flux of non-thermal electrons with low over-lying coronal pressure (or no pre-heating). Note that the HUV and HXR counts in the present study are not converted to physical units. If the conversion involves only a linear transformation, then the two scaling laws are identical.

In summary, the experiments performed indicate that HXR and UV emission rise and peak nearly simultaneously at very short time scales, both likely being produced by the same mechanism of electron precipitation. On the other hand, UV emission exhibits a long gradual decay at the same location, which is not apparently related to the process that produces HXRs. Note that many two-ribbon flares also exhibit apparent motion of UV and HXR sources along the PIL typically at the speed of a few tens to a few hundred kilometers per second. The apparent motion is understood to be due to the spread of reconnection along adjacent field lines, leading to energy deposition and heating of the atmosphere at the feet of newly reconnected field lines. We therefore suggest that such

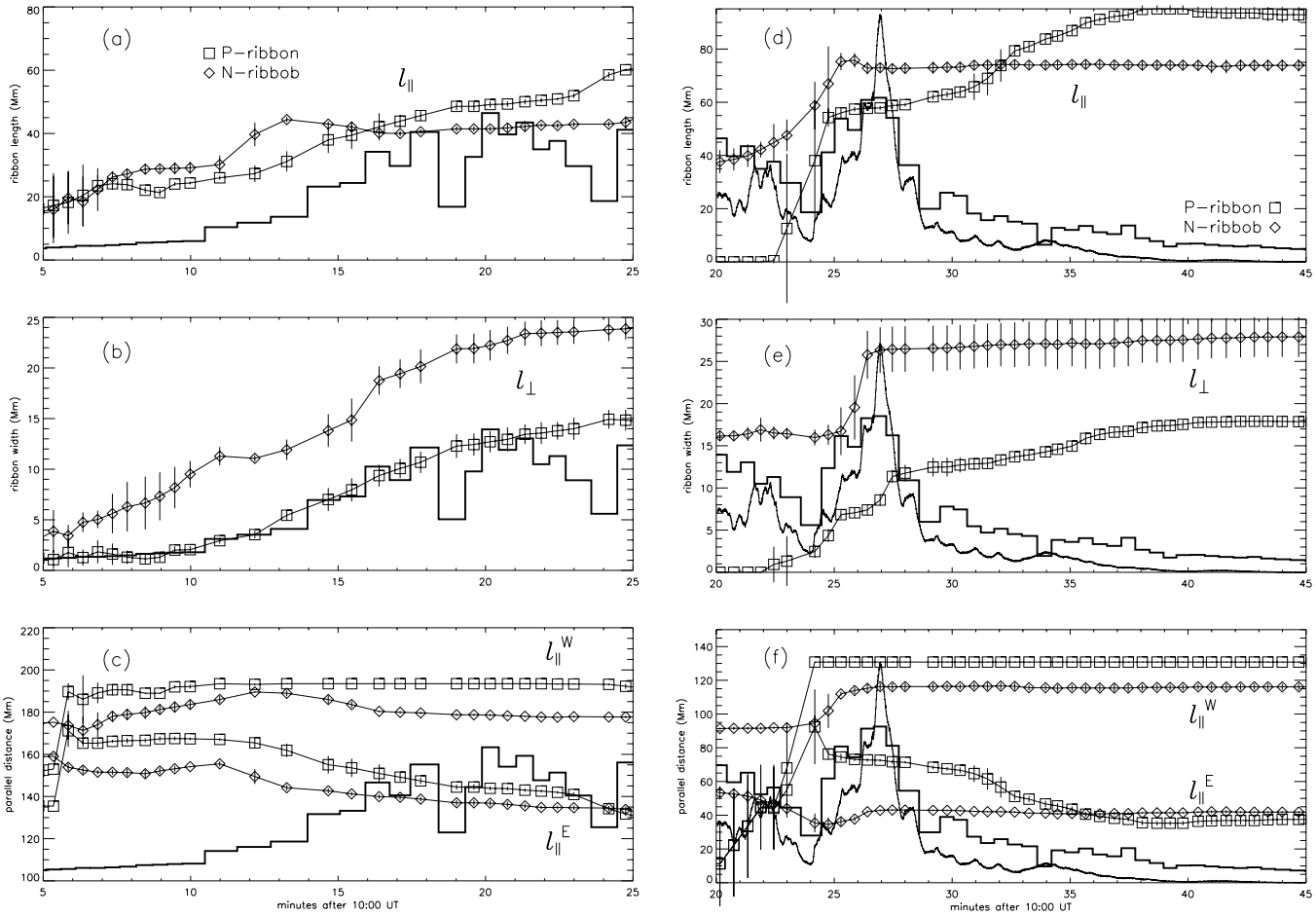

Figure 7. Parallel and perpendicular expansion of UV ribbons during the first phase ((a)–(c)) and the second phase ((d)–(f)). Top: length of the ribbon projected along the PIL. Middle: mean distance of the ribbon front perpendicular to the PIL. Bottom: the parallel distance along the PIL of the "head" (westward) and "tail" (eastward) ribbon fronts. Vertical bars in the plots indicate measurement uncertainties. The thick solid lines indicate HUV light curve arbitrarily normalized, and the thin solid lines indicate HXR (33–53 keV) light curve arbitrarily normalized.

"moving" energization combined with the long "cooling" time in UVs provides a viable explanation, among other plausible interpretations, for the presence of elongated UV two ribbons. Given the characteristic cooling time of 5–10 minutes, it can be estimated that the length of the ribbon is about a few tens of megameters. In the following section, we will further investigate the apparent motion pattern of UV brightening, and how it is related to non-thermal energy release as reflected in radiation signatures.

4. PATTERN OF MAGNETIC RECONNECTION

4.1. Evolution of UV Ribbons

Evolution of flare ribbons in the UV band suggests that the apparent motion of the brightening may be decomposed into motions parallel to and perpendicular to the PIL. Using the method by Qiu (2009), we follow the newly brightened ribbon front in UV emission, and measure its length $l_{||}$ projected along the PIL, the mean distance $l_{\perp}$ of the ribbon front perpendicular to the PIL, and the mean width $w_{\perp}$ of the ribbon as the newly brightened area divided by the ribbon length. Also measured are the distances of the "head" (l^{W}) and "tail" (l^{E}) of the ribbon front projected along the PIL with respect to a fixed position at the PIL. Here we define the "head" of the ribbon front as the westmost end of the ribbon and the "tail" of the ribbon front as the eastern end. The plots show the trajectories of the "head" and "tail" of the two ribbons. In the measurements, the PIL is not assumed to be a straight line; rather it is sketched and described by a best-fit polynomial curve. Note that such measurements are made with an underlying assumption that the pattern of magnetic reconnection is approximately 2.5 dimensional with the translational dimension aligned with the PIL. We regard such an approximation as well justified by the morphology of the two ribbons.

Figure 7 shows the time profiles of these geometric properties overplotted with HUV and/or HXR light curves. Since the flare evolves in nearly two phases at different locations of the active region, we made the measurements for the two phases separately, the first phase being from 10:00 to 10:25 UT, and the second phase from 10:25 to 10:45 UT. The growth of the ribbon length and the mean perpendicular distance of the ribbon front away from the local PIL are plotted in the top and middle panels in the figure. The figures reveal an apparent two-stage evolution of the ribbon motion pattern in both phases. Elongation of the ribbon along the PIL dominates during the rise of the HXR or HUV, which is halted around the peak of HXR/HUV; the perpendicular expansion of the ribbon dominates during the peak and evolves into the decay of HXR and HUV. Note that here the rise, peak, and decay are defined for $\geqslant$25 keV HXRs, different from the traditional definition which refers to soft X-ray emission. The figure shows that even though the reconnection rate precedes the HXR in both

phases, the HXR/HUV peaks when the perpendicular motion dominates. If we consider HXR or HUV as the proxy of the non-thermal energy release rate, the figures show that an energetic process (particularly non-thermal in this study) is associated with not only how much flux is reconnected but the pattern of reconnection reflected in the parallel or perpendicular spread of ribbons.

From the plots, the characteristic mean elongation speed is estimated to be at least several tens of kilometers per second (Figure 7(a)). During the second phase, the positive ribbon in the eastern part of the active region nearly grows instantaneously at a speed of at least a few hundred kilometers per second (Figure 7(d)). Such a motion speed, combined with the long "cooling" time, may be the reason why we see UV emission as extended ribbons, while HXR sources are mostly kernels. The mean perpendicular speed is of order a few kilometers per second, which is smaller by half to one order of magnitude. During the flare evolution in 10 minutes, the perpendicular extension is only a few Mm or a few arcseconds, which can be hardly detected in the HXR imaging observations.

The bottom panels of the figure show the two ends of the flare ribbon evolving in the eastward or westward direction. It is seen that, in both phases, the ribbons in the positive (P-ribbon hereafter) and negative (N-ribbon) magnetic fields start from afar and then approach each other along the PIL. The apparent motion pattern of the flare ribbons indicate evolution of connectivity during the flare. If the connectivity illustrated in the UV ribbons reflects post-reconnection connectivity, the evolution pattern seen in the figure shows that reconnection nearly proceeds in an unshearing manner, with the post-reconnection field lines highly sheared with respect to the PIL initially, and in the later stage, the post-reconnection field line nearly perpendicular to the PIL. Such patterns have been reported in previous studies.

The apparent motion pattern of flare ribbon brightening reflects the evolution of magnetic reconnection between magnetic structures, and the measured geometric properties of the flare ribbons will be related to properties of magnetic reconnection.

4.2. Inferred 2.5 dimensional Pattern of Magnetic Reconnection

The 2.5 dimensional approximation allows us to re-write the reconnection rate ψ as contributed by two parts: $\psi_{\rm rec} \approx \psi_{||} + \psi_{\perp}$, where $\psi_{||} \approx \langle B\rangle l_{\perp}\partial l_{||}/\partial t$ and $\psi_{\perp} \approx \langle B\rangle l_{||}\partial l_{\perp}/\partial t$, referring to reconnection rates due to parallel elongation and perpendicular expansion, respectively. $\langle B\rangle$ indicates the mean magnetic field strength (or flux density) in the newly brightened pixels. These two components are computed from the geometric properties. In the 2.5 dimensional manner, $\psi_{\perp}$ is equivalent to the two-dimensional description of the reconnection rate as the product of the mean reconnection electric field (equivalent to the inductive electric field in the inflow region) $E = \langle B\rangle \partial l_{\perp}/\partial t$ and the length of the current sheet $l_{||}$.

Figures 8(a) and (b) show evolution of the two components of the reconnection rate together with the HXR and HUV light curves, as well as the coronal plasma temperature profile derived from *GOES* two-channel observations. It is immediately seen that the reconnection rate component $\psi_{\perp}$ due to perpendicular expansion now tracks the rise, peak, and decay of the HXR and HUV fluxes during the two phases. This comparison suggests that, if HUV and HXR fluxes are viewed as a proxy for the non-thermal energy release rate, the non-thermal energy release is apparently more efficient when the ribbon perpendicular motion dominates.

We note some other details in the plots. Despite the overall good correlation between $\psi_{\perp}$ and HUV/HXR fluxes, there is no $\psi_{\perp}$ signature at 10:20 UT when HUV and HXR fluxes exhibit a peak. This may be caused by the rigid division of the two phases, which fails to describe the transition between the two phases. For example, the N-ribbon in the east was brightened earlier than 10:25 UT. We also note that at about 10:07 UT, the HUV flux does not exhibit a peak, while there is a peak in both the temperature (of 15 MK) and the reconnection rate profiles. It indicates that this initial phase is associated with strong heating of a small amount of plasma in the corona, but there is no significant heating in the lower atmosphere, either by thermal or non-thermal mechanisms, to give rise to pronounced UV emission. In fact, the peaks in the reconnection rate $\psi_{\perp}$ also coincide with a temperature enhancement in the corona, suggesting that instantaneous heating (within the given cadence of 20–40 s) is also taking place.

We recall that, during the elongation of flare ribbons in both phases, magnetic reconnection seems to proceed in an "unshearing" manner (see Figures 7(c) and (f)). The post-reconnection field lines are more inclined toward the PIL at the start, and then become nearly perpendicular to the PIL in the later stage. Such a phenomenon has been reported in many previous studies of two-ribbon flares. We measure the mean "shear" θ, defined by the inclination of the post-reconnection field lines projected to the plane of sky and with respect to the PIL, as $R \equiv \cot(\theta) = (\langle l_{||}^{P}\rangle - \langle l_{||}^{N}\rangle)/(\langle l_{\perp}^{P}\rangle + \langle l_{\perp}^{N}\rangle)$, where the numerator is the difference between the mean parallel position of the P-ribbon and the mean parallel position of the N-ribbon, and the denominator is the mean perpendicular distance between the P-ribbon and N-ribbon. With a 2.5 dimensional assumption, we may further infer that the measured R is equivalent to the mean ratio B_g/B_o, where B_g is the magnetic field component parallel to the PIL, or the guide field, and B_o is the outflow transverse magnetic field component at the reconnection site in the corona. By 2.5 dimensional assumption, we imply that the guide field component is in a prescribed direction aligned with the PIL, which is presumably also the direction of the reconnection electric field or current sheet. Again, such an assumption may be justified by the morphology and nearly organized evolution pattern of two ribbons. Note that the method described here can only estimate the ratio of the guide field to the outflow transverse field, but not the inflow transverse field, which is the reconnection field component. Since the inflow transverse field is in general greater than the outflow field, the ratio of the guide field over the inflow field should be smaller than the computed R.

Figure 8(c) shows the profile of θ during the first and second phases together with the HXR and HUV fluxes and temperature profiles. Note that these two phases relate to different magnetic structures at two locations of the active region. Also note that we start the measurement from 10:07 UT in the first phase and from 10:24 UT in the second phase, when the ribbon is formed with a well-trackable elongation and expansion pattern. Before these times, the ribbon starts from kernels and expands in both directions to form ribbons of a length much larger than uncertainties. The figure shows that, in both phases, reconnection proceeds with decreasing R or smaller B_g/B_o. This result simply reflects the observation that the evolution of the flare ribbons is "unshearing" and is dominated by perpendicular expansion in the later phase.

The value of R varies from 1.2 to 0.4 during the flare. The ratio of the guide field over the inflow transverse field would be

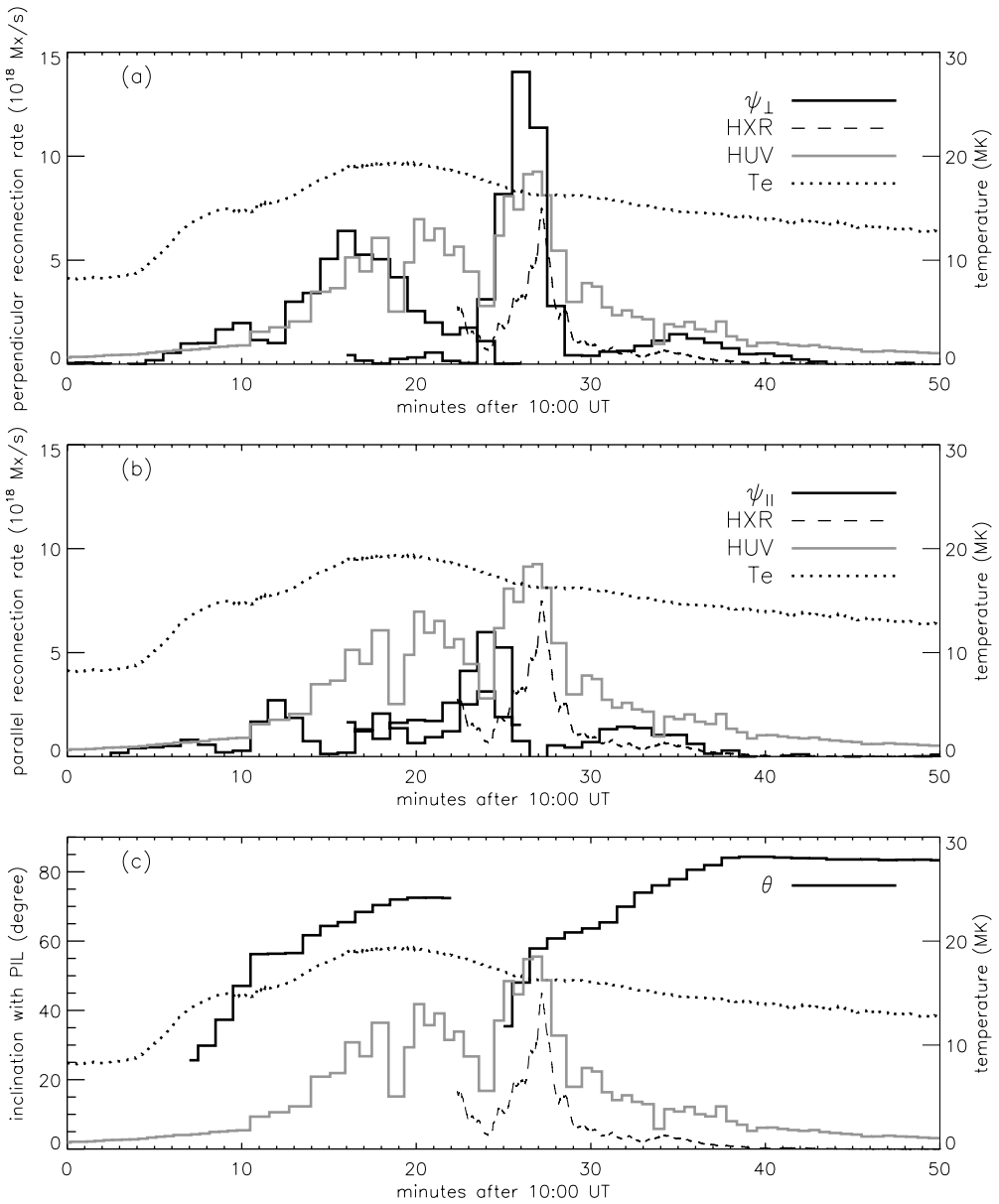

Figure 8. Time profiles of perpendicular reconnection rate (top panel), parallel reconnection rate (middle panel), and guide field in terms of θ (bottom panel) superimposed on HXR (33–53 keV) and HUV light curves and the temperature profile measured from *GOES* two-channel emissions.

smaller than these values. In general, when we compare the two phases, we see that both $\psi_\perp$ and R are greater during the second phase, when the non-thermal emission is stronger. We also note that in both phases, the direction of the guide field $\vec{B}_g$ (from the positive to the negative) is parallel to the reconnection electric field $\vec{E}$ as indicated by the sign of R.

To sum up, the comparison of time profiles of flare radiation signatures and properties related to magnetic reconnection inferred from geometric properties of flare UV ribbons (in a 2.5 dimensional approximation) suggests that instantaneous energy release (thermal or non-thermal) is more closely related to the perpendicular expansion of flare ribbons, when the outflow transverse field relative to the guide field is greater.

We recall that, in reality, any two field lines meeting at a reconnection site naturally have parallel (guide field) and anti-parallel (reconnection field) components, but it is in general difficult to determine from observations in the guide field direction. In the present study, we assume the guide field to be directed along the PIL, which may be justified by the two-ribbon morphology and organized ribbon motion. Also note that in the present study, we only capture the global mean pattern of post-reconnection connectivity between two sources, the positive ribbon and the negative ribbon. A more precise measurement of the shear or guide field is necessary when spatially resolved three-dimensional connectivity between individual field lines can be determined (see Qiu 2009). The presence of the guide field modifies the physics of reconnection as well as energy release (e.g., Longcope et al. 2010), as will be briefly discussed in the next section.

5. DISCUSSION

5.1. The Role of the Guide Field

The role of the guide field in reconnection may be viewed in two parts: how the guide field may change the reconnection rate

and how it may trigger fast reconnection. The reconnection rate quantifies how quickly magnetic flux flows into the diffusion region, and is often described by the asymptotic inductive electric field E. Numerical simulations in 2.5 dimensions in both collisional and collisionless regimes (e.g., Birn & Priest 2007) show that the reconnection rate E is barely modified by a moderate guide field ($B_g/B_i \leqslant 1$) (Swisdak et al. 2005; Pritchett 2006), suggesting that the global dynamics rather than microscopic physics govern the reconnection rate. However, the role of the guide field in triggering fast reconnection is discussed by Drake (2003), Drake et al. (2006), and Cassak et al. (2007) since it ties electrons to the current sheet and produces current instabilities that lead to fast reconnection. In these scenarios, it should be understood that the role of the guide field is to trigger fast reconnection, which then carries on as governed by the global dynamics.

The observations showing that reconnection starts with a relatively strong guide field may suggest that a strong guide field is in favor of microscopic instabilities related to electrons tied into the current sheet, thus triggering fast reconnection. The perturbation propagates along the current sheet, giving rise to the parallel motion of flare ribbon brightenings. In general, the characteristic speed of such a spread would be comparable to the Alfvén speed in the current sheet, the estimate of which is hard since both the magnetic field (the guide field) and density are unknown and are very likely quite different from those in the average active region corona.

The guide field topology is also directly related to particle acceleration. In an illuminating paper, Litvinenko (1996) shows that the guide field will tie electrons inside the reconnection current sheet thus increasing the kinetic energy of the particle to that it far exceeds the drift speed before it is finally ejected out of the X-line current sheet. The maximum particle energy in the given setup is $\sim B_{||}/B_{\perp}E$ for a given constant reconnection rate E. Further, different from the case of perpendicular acceleration ($\vec{E} \perp \vec{B}$), acceleration with a guide field gives more energy to electrons. While this analytical frame work only describes single particle motion and ignores the particle field interaction which determines E self-consistently, recent 2.5 dimensional particle-in-cell simulations suggest that electron acceleration (within the simulation cell) is primarily achieved by an inductive electric field E either at the X-line or in the flux pile-up regions, depending on the presence of the guide field (Pritchett 2008). Some particle-in-cell simulations, though different in some details, showed that with a moderate guide field ($B_g/B_i \approx 1$), particle energization goes through two stages. During the first stage, the energization mainly takes place along the X-line and is not significant in terms of the energy gain by electrons, and in the second stage, acceleration of electrons involves magnetic islands by either electrons colliding with magnetic islands through a Fermi-type mechanism (Drake 2003) or direct acceleration in electron holes formed along the X-line (Pritchett 2008). The second stage would favor a large particle acceleration since the acceleration region is not confined to the X-point. In the case of multiple island acceleration, effective ejection of particles out of the X-line into these islands would require a weak guide field. Furthermore, with a guide field, the electron pitch angle distribution is largely modified, as shown in simulations by Pritchett (2008). Without a guide field, the accelerated electrons initially exhibit a perpendicular acceleration (indicating that the inductive electric field is perpendicular to the magnetic field), and the pitch angle distribution peaks at 90°. With the guide field, an electron undergoes parallel or anti-parallel acceleration with a very small pitch angle nearly along the guide field direction. These differences in properties of accelerated particles would be ultimately reflected in HXR and HUV radiation signatures.

5.2. Properties of Electron Precipitation Site

The time profile analysis in the last section shows that UV emission rises and peaks together with HXRs, suggesting that prominent UV enhancement is due to precipitating electrons that give rise to UV and HXR emissions simultaneously. Indeed, at any given interval, it is found that HXR sources from the reconstructed HXR maps are located at the brightest UV sources. The HXR map reconstruction with a nominal 5–10″ resolution, however, compromises the accurate spatial information, such as the exact location and source size of electron precipitation sites. We therefore carry out an experiment to draw insight from HUV images that are integrated for every 2 minutes.

The top panels in Figure 9 show the histogram of HUV areas as a function of HUV counts (as a fraction of the maximum counts of 3×10^5 DN s^{-1}; allowing this maximum value to vary certainly changes the distribution, but not significantly) for two time intervals when HUV and/or HXR peaks. In the plot, we distinguish footpoints in the positive magnetic field from footpoints in the negative magnetic field. It is seen that, in general, the negative brightening is more dispersed in larger areas. If we only look at the brightest regions (larger than 50% of the maximum), the area can be as small as 20 arcsec^2, or 4–5 arcsec in size. At the intensity level of $\geqslant$13%, the area is between 100–200 arcsec^2, or 10–14 arcsec in size. Note that these images are integrated for 2 minutes (three to four time frames given the image cadence), the HUV kernel sizes above give upper limits of the size of the footpoints where electrons precipitate instantaneously. We further estimate the electron flux to be $F_{\rm nth} \approx 4 \times 10^{26} C_{M1}$ erg s^{-1}, where C_{M1} is the counts rate at the HXT-M1 channel, and $F_{\rm nth}$ stands for non-thermal flux in units of erg s^{-1} (Aschwanden et al. 1999). At the peak of the flare, C_{M1} is about 900 DN s^{-1}; therefore, the non-thermal energy flux at the precipitating site ranges from $10^{11.5}$ to $10^{12.5}$ erg s^{-1}cm^{-2}, placing the heating regime in explosive heating of the lower atmosphere. If, however, we only count the non-thermal flux from 40 keV, then the scaled down flux is smaller by about one order of magnitude, still a very large non-thermal flux.

From the middle and bottom panels, it is also seen that, in general, the total HUV flux in negative fields is larger, whereas the mean magnetic field is stronger, qualitatively in agreement with the scenario of magnetic mirroring effect (Melrose & White 1981) if we treat the flare geometry as just one grand positive patch connected with the grand negative patch. On the other hand, in detail, we also find that stronger HUV flux locates at a stronger magnetic field—here we only compare positive with negative as the mirroring effect only refers to conjugate footpoints. During the 26–28 minute (the peak in HXR and HUV), HUV flux in the positive field is stronger, whereas the magnetic field is also stronger. This is also reported earlier by Fletcher & Hudson (2001) from the HXR maps (see their Figure 10).

We note, however, that the direct comparison of flux and the magnetic field at the strongest HXR or HUV sources do not really verify or disprove the mirroring effect, as the connectivity is unknown, particularly when multiple post-reconnection flux tubes are involved. Instead, we look into HUV images to take into account all emitting sources. Ideally, if prominent HUV emission is produced by precipitating electrons and is governed by the mirroring effect in the case of strong diffusion, the

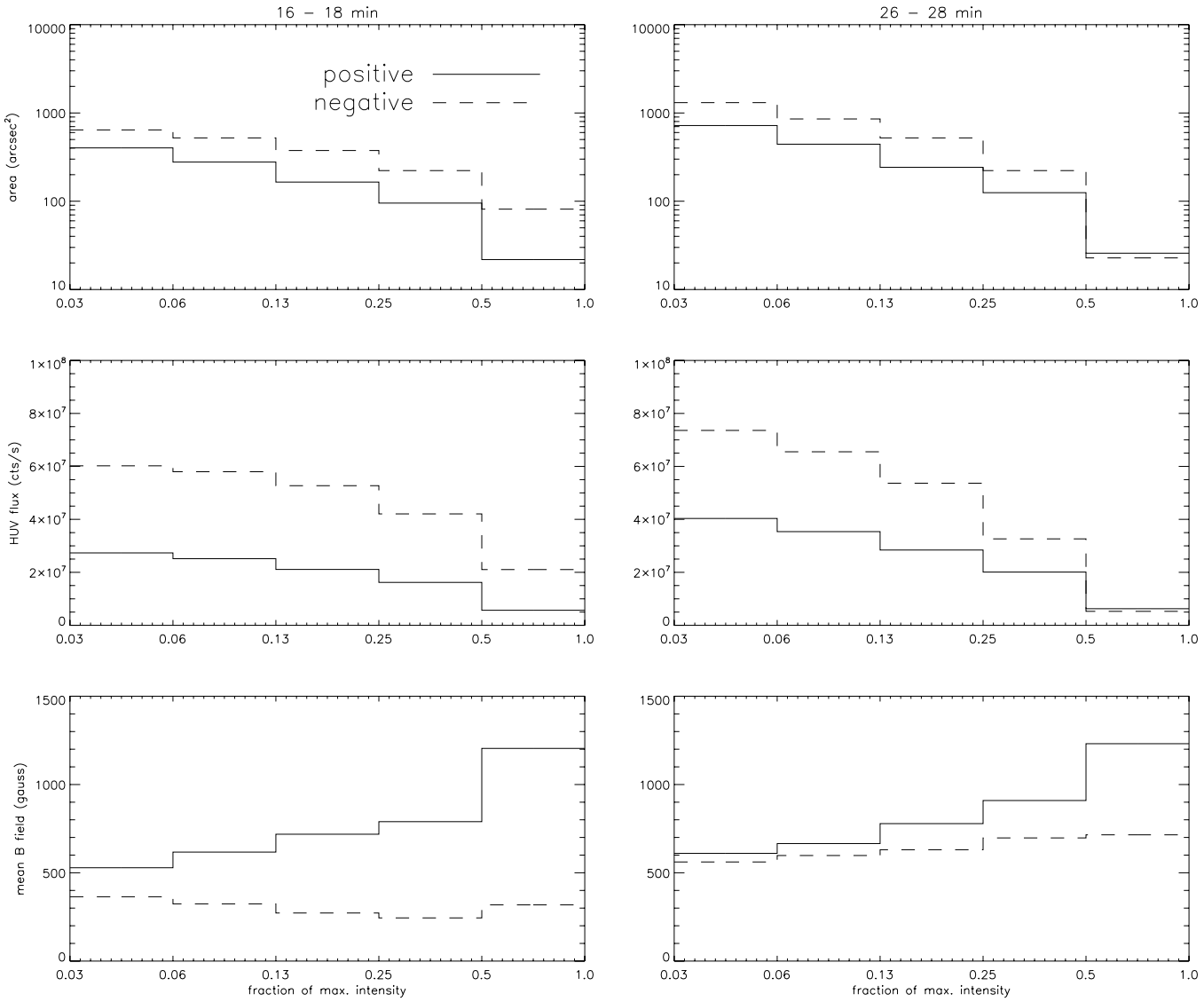

Figure 9. Statistics of the area, HUV flux, and mean magnetic field of pixels with the HUV brightness above a certain cutoff value (in terms of fractions of a fixed maximum value) for two time intervals during the peaks of HXR/HUV. Solid lines indicate pixels in the positive magnetic field, and dashed lines indicate pixels in the negative magnetic field.

product $F_{\rm nth}B$ of non-thermal flux $F_{\rm nth}$ and magnetic field B in any positive footpoint will be the same as in the conjugate negative footpoint. Without knowing individual connectivity, it is expected that the histogram of $F_{\rm nth}B$ at all sources in the positive field is the same as the histogram in the negative field, assuming that the size of the flux tube is not larger than a pixel ($1''$ in this study). Figure 10 shows such histograms for the two intervals when HUV and/or HXR peaks. The top panel shows the $F_{\rm HUV}B$ distribution, and the bottom panel shows the $F_{\rm HUV}^{1.67}B$ distribution, considering that the HUV and HXR fluxes are scaled roughly by $F_{\rm HUV} \sim F_{\rm HXR}^{0.6}$ (see Section 3.2 as well as McClymont & Canfield 1986). This later rendition does not change the shape of the histogram. We see that the distribution in the positive field is certainly different from that in the negative field, and for this flare, at both peaks, the stronger positive field also has stronger HUV flux, as indicated by the high FB tail of the positive distribution.

There are many ways that may dictate the flux scaling in conjugate footpoints. The mirroring effect is the best known, and the approximate scaling law used above is based on the assumption of strong diffusion that produces isotropic electron pitch angle distribution. It is suggested, however, that electrons accelerated by an inductive electric field during reconnection with a non-negligible guide field would rather exhibit an anisotropic pitch angle distribution, depending on whether the inductive E field is parallel or anti-parallel to the guide field. If the guide field is parallel to the inductive electric field, and without considering scattering, electrons will be seen precipitating primarily into the positive magnetic field regardless of the strength of the field. We note that the observations are consistent with such a scenario, that the reconnection electric field $\vec{E}$ is parallel with the guide field $\vec{B}_g$, and the HUV flux in the positive field is also larger. Note that this scenario certainly ignores scattering after acceleration at the reconnection site. However, this may be justified as energization of electrons takes place in newly formed post-reconnection flux tubes before the onset of chromosphere evaporation to raise the plasma density in the tube.

5.3. Conclusions

The re-visit of the Bastille-day two-ribbon flare gives new insights into magnetic reconnection and energy release. A

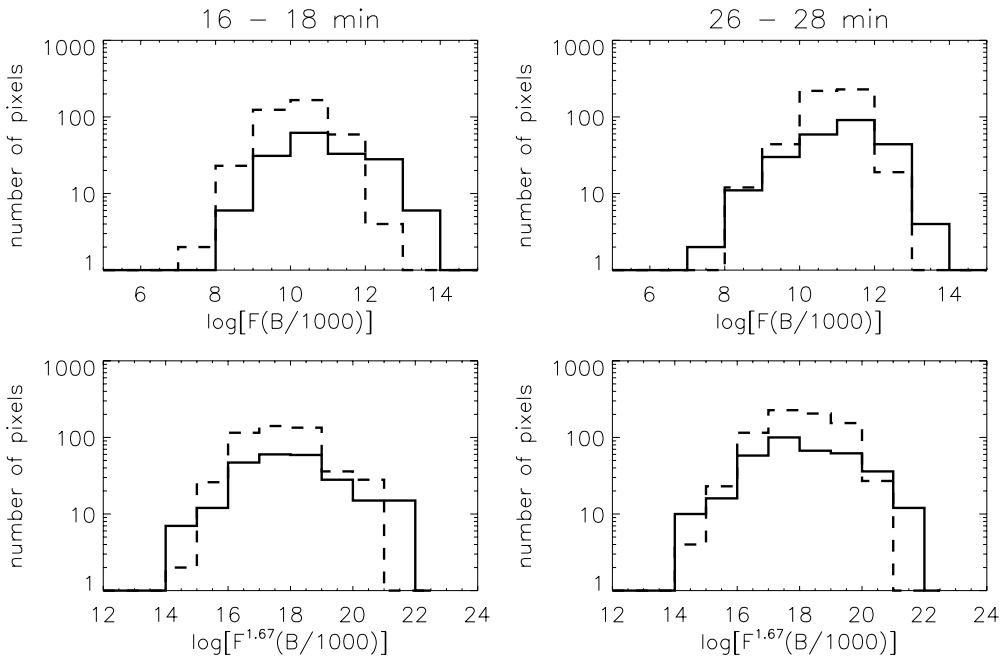

Figure 10. Histograms of $F^{\alpha}B$ ($\alpha \geqslant 1$) of bright HUV pixels in positive (solid line) and negative (dashed line) magnetic fields (see the text). F refers to calibrated HUV counts per second and B is the magnetic flux density in each pixel.

semi-quantitative analysis of HXR and UV observations leads to answers to the two questions raised at the start of the study. We confirm that HXR and prominent UV emissions are both produced primarily by precipitating electrons along newly reconnected field lines. Also, reconnection and subsequent energy release along adjacent field lines along the PIL (the so-called zipper effect) combined with elongated decay of UV emission may provide a viable explanation, among many, for the observed extended UV ribbons, whereas HXR sources with rapid decay appear mostly as compact kernels. Though beyond the scope of this study, the elongated decay in UV emission is itself an interesting topic, and an understanding of this may invoke radiative hydrodynamic modeling of lower-atmosphere heating as well as investigation of continuous heating mechanisms in the post-reconnected flux tube after instantaneous non-thermal energy deposition.

We also measured geometric properties of UV flare ribbons, which, in a 2.5 dimensional approximation, is used to infer the pattern of magnetic reconnection in terms of reconnection with a guide field in a prescribed direction along the PIL. It is shown that the HXR emission, as a first-order proxy of non-thermal energy flux, is strongly correlated with the component of the reconnection rate $\psi_{\perp}$ due to a dominant perpendicular spread of the flare ribbon with respect to the PIL. In other words, the efficiency of instantaneous non-thermal energy release is related to the pattern of reconnection, which may be viewed, in a 2.5 dimensional approximation, as reconnection with an ever decreasing guide field relative to the reconnection outflow field $B_g/B_o \sim 1.2 - 0.4$. The presence of the guide field modifies the physics of magnetic reconnection as well as particle energization, as might be reflected in the present study.

Taking advantage of high-resolution UV observations, we also experimentally explore properties of electron precipitation sites. The analysis suggests that electrons are probably injected into kernels of area 20–200 arcsec^2. This gives rise to a very high precipitating electron beam density and produces explosive heating of the chromosphere during the flare. Furthermore, we made a simple experiment to test the magnetic mirroring effect, and the observed scaling between non-thermal flux and magnetic field strength at the footpoints does not always obey the scaling law based on mirroring with an isotropic pitch angle distribution. Instead, we note that during HXR emission peaks, more intensive non-thermal flux deposit in the foot regions of the positive magnetic field which is likely stronger than its conjugate negative field. Such a result is qualitatively consistent with electron acceleration with a guide field parallel to the reconnection electric field, in which case, electrons have an anisotropic pitch angle distribution and predominantly precipitate at the positive field regardless of the field strength, if post-acceleration scattering effects are justifiably ignored. This issue awaits further testing with observations of better quality in both UV and HXRs, as well as resolved connectivity.

Admittedly, the analyses and subsequent conclusions in the present study are mostly qualitative as a result of compromised observational capabilities. We intentionally avoid imaging and spectral analysis of HXR observations being aware of the large uncertainties associated with these practices. The UV observation of this event suffers from varying (and very short) exposures causing undetermined nonlinear effects on the photometry analysis. However, such experiments may be pursued with observations of better quality—higher (and even) cadence, UV photometry with improved calibration and knowledge of its radiation mechanism, and HXR imaging and spectral observations with adequate resolution (such as those provided by SDO and *RHESSI*; Lin et al. 2002))—and advanced analysis tools such as determination of resolved three-dimensional connectivity between individual flux tubes or flux domains in the very least (Qiu 2009).

We thank Drs. R. W. Nightingale and T. Tarbell for help with *TRACE* calibration. The work benefits from illuminating discussions with Drs. D. Longcope, E. Priest, P. Martens, and R. C. Canfield. We thank the referee whose constructive comments

helped improve the clarity of the manuscript. We acknowledge the *TRACE*, *SOHO*, and *Yohkoh* missions for providing quality observations, and the *Yohkoh* Legacy Data Archive for prompt user support. This work is supported by NSF grant ATM-0748428 and NASA grant NNX08AE44G. Part of the data analysis work was conducted under the support of the NSF REU program at MSU with the grant ATM-0552958.

REFERENCES

Aschwanden, M. J., Kosugi, T., Hanaoka, Y., Nishio, M., & Melrose, D. B. 1999, ApJ, 526, 1026
Barnes, G., Longcope, D. W., & Leka, K. D. 2005, ApJ, 629, 561
Birn, J., Fletcher, L., Hesse, M., & Neukirch, T. 2009, ApJ, 695, 1151
Birn, J., & Priest, E. R. (ed.) 2007, Reconnection of Magnetic Fields: MHD and Collisionless Theory and Observations (Cambridge: Cambridge Univ. Press)
Bogachev, S. A., Somov, B. V., Kosugi, T., & Sakao, T. 2005, ApJ, 630, 561
Cassak, P. A., Drake, J. F., & Shay, M. A. 2007, Phys. Plasmas, 14, 054502
Des Jardins, A. C. 2007, PhD thesis, Montana State Univ.
Drake, J. F. 2003, Science, 299, 873
Drake, J. F., Swisdak, M., Che, H., & Shay, M. A. 2006, Nature, 443, 553
Fletcher, L., & Hudson, H. 2001, Sol. Phys., 204, 69
Foukal, P. V., & Behr, B. B. 1995, Sol. Phys., 156, 293
Grigis, P. C., & Benz, A. O. 2008, ApJ, 683, 1180
Handy, B. N., et al. 1999, Sol. Phys., 187, 229
Jing, J., Qiu, J., Lin, J., Qu, M., Xu, Y., & Wang, H. 2005, ApJ, 620, 1085
Kazachenko, M. D., Canfield, R. C., Longcope, D. W., Qiu, J., Des Jardins, A., & Nightingale, R. W. 2009, ApJ, 704, 1146
Kitahara, T., & Kurokawa, H. 1990, Sol. Phys., 125, 321
Kosugi, T., et al. 1991, Sol. Phys., 136, 17
Krucker, S, Fivian, M. D., & Lin, R. P. 2005, Adv. Space Res., 35, 1707
Lee, J., & Gary, D. E. 2008, ApJ, 685, 87L
Lin, R. P., et al. 2002, Sol. Phys., 210, 3
Litivinenko, Y. E. 1996, ApJ, 462, 997
Longcope, D. W., Beveridge, C., Qiu, J., Ravindra, B., Barnes, G., & Dasso, S. 2007, Sol. Phys., 244, 45
Longcope, D. W., Des Jardins, A., Carranza-Fulmer, T., & Qiu, J. 2010, Sol. Phys., in press
McClymont, A. N., & Canfield, R. C. 1986, ApJ, 305, 936
Melrose, D. B., & White, S. M. 1981, J. Geophys. Res., 86, 2183
Moore, R. L., Sterling, A. C., Hudson, H. S., & Lemen, J. R. 2001, ApJ, 552, 833
Neupert, W. M. 1968, ApJ, 153, L59
Poletto, G., & Kopp, R. A. 1986, in The Lower Atmosphere of Solar Flares, ed. D. F. Neidig (Sunspot, NM: NSO/Sacramento Peak), 453
Pritchett, P. L. 2006, J. Geophys.cal Res., 111, A10212
Pritchett, P. L. 2008, Phys. Plasmas, 15, 102105
Qiu, J. 2009, ApJ, 692, 1110
Qiu, J., Lee, J., Gary, D. E., & Wang, H. 2002, ApJ, 565, 1335
Qiu, J., Wang, H., Cheng, C. Z., & Gary, D. E. 2004, ApJ, 604, 900
Saba, J. L. R., Gaeng, T., & Tarbell, T. D. 2006, ApJ, 641, 1197
Sakao, T. 1994, PhD thesis, Univ. Tokyo
Sato, J., Kosugi, T., & Makishima, K. 1999, PASJ, 51, 127
Solar Physics Special Issue 2001, Vol. 204, issue 1/2 (Dordrecht: Kluwer)
Su, Y., Golub, L., & van Ballegooijen, A. A. 2007, ApJ, 655, 606
Swisdak, M., Drake, J. F., Shay, M. A., & McIlhargey, J. G. 2005, J. Geophys. Res., 110, A05210